# Optical second harmonic signature of phase coexistence in ferroelectric|dielectric heterostructures

Nives Strkalj [1,*] Amadé Bortis [1], Marco Campanini,[2] Marta D. Rossell [2] Manfred Fiebig [1], and Morgan Trassin [1]

[1]*Department of Materials, ETH Zurich, 8093 Zurich, Switzerland*

[2]*Electron Microscopy Center, Swiss Federal Laboratories for Materials Science and Technology, Empa, Dübendorf 8600, Switzerland*

An exotic coexistence of polar states is known to occur in ferroelectric|dielectric $PbTiO_3$|$SrTiO_3$ (PTO|STO) heterostructures. In the PTO layers with a thickness of 10–20 unit cells, in-plane-polarized regions order alongside the so-called vortex phase with a whirl-like arrangement of electric dipoles. We investigate the optical signature of these polar phases noninvasively using optical second harmonic generation (SHG) on PTO|STO-based heterostructures. We identify the phase coexistence down to a single PTO|STO bilayer. By comparing the SHG yield in dependence of the number of PTO layers, we further find that interlayer coupling plays an important role in setting the final polarization state. Our nonlinear optical experiments demonstrate the potential of this noninvasive approach for the identification and understanding of complex noncollinear ordering of dipole moments in oxide heterostructures and lays the groundwork for their operando investigation.

## I. INTRODUCTION

Complex polar phases consisting of nanoscale arrays of electric dipole moments that exhibit a continuous spatial change in orientation were recently observed in ferroelectric|dielectric $PbTiO_3$|$SrTiO_3$ (PTO|STO) heterostructures [1–16]. In these complex polar phases, local negative capacitance was measured, which is considered to be a powerful new ingredient in transistor technology. Ferroelectric|dielectric heterostructures are, thus, becoming a promising platform for oxide-electronic applications [17–21]. Current investigations on the PTO|STO system involve scanning transmission electron microscopy (STEM) in combination with x-ray diffraction (XRD) or piezoresponse force microscopy (PFM). In contrast to the investigation of conventional polar phases, the investigation of complex polar phases using XRD and PFM often requires a superlattice architecture because this increases the sample volume so that signals become measurable. In turn, the difficulty to identify noncollinear ordering of dipole moments noninvasively and in technologically relevant single layers prevents a deeper understanding of the formation of complex phases in these and their integration into devices.

Here we show that optical second harmonic generation (SHG) is an ideal tool for noninvasive access to the complex arrangement of dipole moments in PTO|STO heterostructures. Our symmetry analysis of the SHG polarimetry in a PTO|STO superlattice and a single STO-capped PTO layer reveals the presence of distinct SHG contributions from two polar phases. We specifically identify the coexistence of a ferroelectric multidomain phase with in-plane polarization ordering and a polar vortexlike phase exhibiting a net in-plane polarization. Furthermore, an oscillatory evolution of the SHG yield with the number of deposited PTO and STO constituent layers points to a previously overlooked coupling effect between the PTO layers. We find an antiparallel configuration of the in-plane polarized domains between adjacent layers which attenuates the net in-plane polarization. We believe that our noninvasive approach expedites the search for complex polar phases and the study of their time-dependent operando response to electric fields.

## II. METHODS

Using a KrF (248 nm) excimer laser, we grew our PTO|STO heterostructures on single-crystalline (110)-oriented $DyScO_3$ (DSO) substrate (Crystec GmbH) with a miscut of $0.1°$, buffered by 4-nm-thick (001)-oriented $SrRuO_3$ (SRO). After optimizing the growth conditions, the SRO layer was deposited at $700\,°C$ in an $O_2$ pressure of 0.1 mbars at a laser fluence of 0.9 J cm$^{-2}$ and a repetition rate of 2 Hz. The PTO and STO layers were deposited at $550\,°C$ in an $O_2$ pressure of 0.12 mbars at a laser fluence of 1.14 J cm$^{-2}$ and a repetition rate of 4 and 2 Hz, respectively. Simultaneously, reflection high-energy electron diffraction (RHEED) is performed to ensure the growth quality and calibrate the film thickness with unit-cell accuracy in the Supplemental Material [22]. A Pb-enriched target ($Pb_{1.2}TiO_3$) was used to achieve the layer-by-layer growth mode for RHEED monitoring. The sample was cooled at 10 K/min in the oxygen growth atmosphere. Unit-cell-flat topography of the heterostructures is observed by atomic force microscopy in the Supplemental Material [22]. Crystallographic directions, henceforth, refer to the pseudocubic axes of the DSO substrate.

Samples for the STEM analysis were prepared as cross sections of the films by mechanical polishing, followed by ion milling with grazing incident Ar$^+$ ions using a Fischione Model 1050 TEM-Mill. STEM was performed on a FEI

*ns851@cam.ac.uk

174101-1

Titan Themis equipped with a probe CEOS DCOR spherical aberration corrector operated at 300 kV. A probe convergence semiangle of 25 mrad was used in combination with a collection angular range for the high-angle annular dark field (HAADF) detector set to 90–170 mrad. The HAADF-STEM image used for polarization mapping was obtained from averaging a time series consisting of ten frames, followed by rigid as well as nonrigid registration using the SMART ALIGN software [23]. The time-averaged signal was denoised using a custom-developed nonlinear algorithm based on the method proposed by Du [24]. The atomic-scale polarization mapping was carried out by fitting the position of the atomic columns in the HAADF-STEM image. The picometer-precision fitting was performed by using seven-parameter two-dimensional Gaussians and a custom-developed MATLAB code based on the method proposed by Yankovich *et al.* [25] Then, the polarization map was derived from the relative displacements of the two cation sublattices present in the PTO or STO perovskite-type structures. As the Ti cations are displaced along with the O octahedra, the displacement vector can be determined by measuring the polar displacement on the image plane of the Ti position from the center of mass of its four nearest Pb or Sr neighbors. In the polarization map derived from HAADF-STEM image, the dipole moments are plotted opposite to the displacement of the Ti cations.

For the frequency-doubling SHG measurements, the incident light was generated by a Ti:sapphire laser light with a pulse duration of 45 fs, a repetition rate of 1 kHz, and a wavelength of 800 nm, which was converted using an optical parametric amplifier to light with a wavelength of 1200 nm. This incident beam with a pulse energy of 30 $\mu$J and a fluence of 0.06 J cm$^{-2}$ was focused onto the sample to a spot with a diameter of 250 $\mu$m. The optical SHG signal was generated at 600 nm and detected using a monochromator and a photomultiplier system.

## III. RESULTS

### A. Characterization of ordering of dipole moments in the PTO|STO superlattice

A (PTO|STO)$_8$PTO superlattice where each constituent layer has a thickness of 12 unit cells was synthesized as described in Sec. II. This particular type of PTO|STO superlattice has been shown to host a phase coexistence of: (i) a so-called $a_1/a_2$ phase and (ii) a vortex phase in the PTO layers [5,9]. (i) In the $a_1/a_2$-phase, domains with a polarization along [100] or [010], termed $a_1$ and $a_2$ domains, respectively, arrange in alternating stripes. (ii) In the vortex phase, long-range ordered arrays of electric dipole vortex structures [26] extend in a tubular way along [100]. In addition to the vortexlike arrangement of dipole moments around the vortex core, the resulting tubuli exhibit a net polarization along their central axis in the [100] direction. More details on the polarization configuration in the vortex phase have been reported elsewhere [27].

We first confirm the phase coexistence of the $a_1/a_2$ phase and the vortex phase in our superlattice using a combination of PFM and XRD, see details in the Supplemental Material [22]. Here the sample response is averaged over the entire thickness
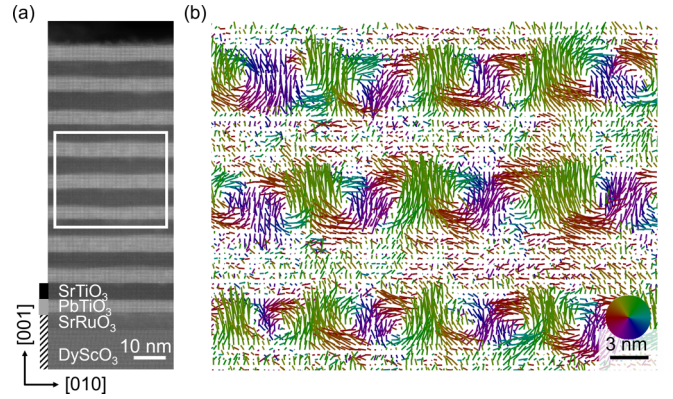


FIG. 1. (a) Atomically resolved HAADF-STEM image of a PTO|STO (gray|black) superlattice on the SRO-buffered (110)-oriented DSO substrate (upward hatching). (b) Postdeposition STEM map of dipole moments in the area outlined in white in (a). The lines show the direction (color wheel) and amplitude (line length) of the dipole moments.

of the superlattice heterostructure. We specifically verify the presence of the vortex phase by cross-sectional STEM imaging, see Figs. 1(a) and 1(b). We map the spatial distribution of the electric dipole moments within the superlattice in the plane perpendicular to the tubular axes of the vortices. We find the expected signature of the vortex phase, that is, a noncollinear arrangement of dipole moments into a circle around the vortex core with alternating vorticity in neighboring whirls within each PTO layer [3].

Let us now move on to the optical characterization of the polar phases in this PTO|STO superlattice by SHG. SHG denotes frequency doubling of a light wave in a material, a process that in its leading order is permitted in the absence of inversion symmetry. This makes SHG an efficient tool for the investigation of ferroelectricity at sample thicknesses down to a single unit cell [28–41]. Furthermore, the insertion of the bottom electrode is not required for detecting polarization by SHG, in contrast to PFM. SHG can only access the inversion-symmetry breaking in the plane perpendicular to the wave vector of the propagating light. We can, therefore, selectively access the in-plane polarization of our heterostructures by choosing a normal-incidence geometry [41,42]. Here, we access the in-plane polarization of our heterostructures by choosing a normal-incidence geometry [41,42] with independent selection of the polarization of the incoming light and the outgoing light parametrized by the angles $\alpha$ and $\beta$, respectively, as depicted in Fig. 2(a). To the best of our knowledge, the only optical SHG report on PTO|STO superlattices [5] was conducted in a near-field geometry in which the independent selection of polarization of the incoming and outgoing light is impossible, thus, preventing a detailed polarimetry analysis. We use a laser spot size of 250 $\mu$m which by far extends beyond the characteristic length scales of the phase separation into the $a_1/a_2$ phase and the vortex phase (about $0.5 \times 5$ $\mu$m$^2$), see the PFM image in the Supplemental Material [22]. Our SHG response is, thus, representative of a statistical mix of coexisting phases in the sample. The polarization of the incoming light is rotated by an angle $\alpha$ ranging
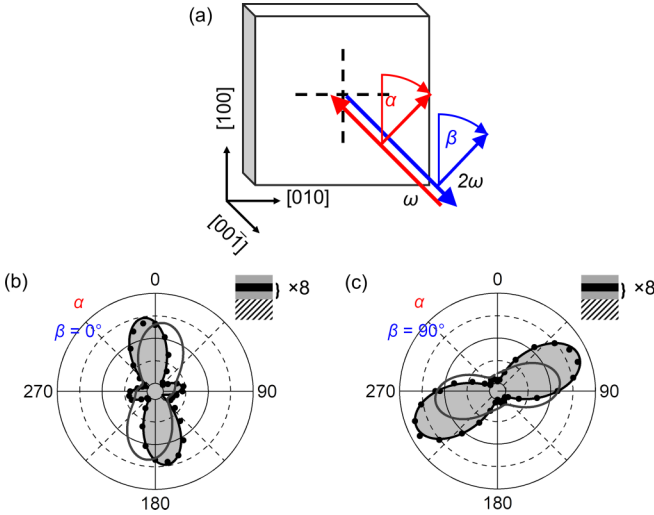
FIG. 2. (a) Schematic of the SHG setup in the employed normal-incidence geometry. Crystallographic directions refer to the pseudocubic axes of the DSO substrate. The incoming light propagates along [001] at 1.033 eV with a linear polarization set to the angle $\alpha$. The generated nonlinear signal at 2.066 eV is analyzed in its polarization state using an analyzer fixed to the angle $\beta = 0°$. (b) and (c) Polar plots of the SHG intensity (points) versus the incident-light polarization angle $\alpha$ for a PTO|STO superlattice with (b) $\beta = 0°$ and (c) $\beta = 90°$. Gray lines are fits of the one-phase model based on Eq. (4), and black lines are fits of the two-phase model based on Eq. (9). A schematic of the heterostructure is given as inset on the top right. Gray denotes PTO, black denotes STO, and upward hatching denotes the SRO-buffered DSO substrate. The intensity scale is equal in (b) and (c).

from 0° to 360°, and the outgoing light is detected at a fixed polarization, that is, $\beta = 0°$ and $\beta = 90°$ with respect to [100] in the SHG polarimetry in Figs. 2(b) and 2(c), respectively.

We observe a pronounced SHG signal indicating a nonzero in-plane net polarization. Extracting the details of the polar order in our superlattice from the SHG polarimetry data is difficult because of the coexistence of two different polar phases. These phases are expected to have a different spectral dependence, i.e., a unique relative value of SHG tensor components for each fundamental wavelength and in each phase. Furthermore, the SHG responses of the $a_1/a_2$ phase and the vortex phase interfere in an undetermined way. This complexity manifests itself, for example, in the polarization angle of the incoming light at which we observe maximum SHG yield, see Figs. 2(b) and 2(c). In contrast to simpler one-phase systems [35,36,42,43], this direction does not coincide with the direction of the spontaneous net polarization along one of the optical principal axes. To evaluate the polar configuration of our system from the SHG polarimetry, it is, therefore, necessary to model the SHG response in greater detail than before.

## B. Modeling of the SHG response of PTO|STO heterostructures

To model our polarimetry results, we consider the general expression for the leading-order SHG contribution,

$$P_i^{(2)}(2\omega) = \epsilon_0 \chi_{ijk}^{(2)} E_j(\omega) E_k(\omega), \tag{1}$$

where $E(\omega)$ is the incoming light field, $P^{(2)}(2\omega)$ is the nonlinear polarization induced in the material, and the tensor $\hat{\chi}^{(2)}$ is linked to the point-group symmetry of the crystal. The indices $i$, $j$, and $k$ refer to the $x \parallel a$, $y \parallel b$, $z \parallel c$ axes of a Cartesian coordinate system adopted to the *local* orientation of the unit cell.

The $4mm$ point-group symmetry describes both the $a_1/a_2$ phase and the net polarization of the vortex phase in tetragonal PTO. In the $4mm$ point-group symmetry, $z$ denotes the fourfold axis which is the local direction of the spontaneous polarization, and only the tensor components $\chi_{zxx} = \chi_{zyy}$, $\chi_{zzz}$, and $\chi_{xzx} = \chi_{yzy}$ can be nonzero [44]. We measure the angular dependence of the SHG intensity in a *global* coordinate system of the substrate as defined by the axes [100], [010], and [001] introduced in Fig. 2(a). We relate the SHG contributions described in the local coordinate system of the unit cell to the global coordinate system of the sample by accounting for the rotation of the unit cell in the local coordinate system with respect to the global coordinate system and then projecting the SHG contributions along the directions of the global coordinate system given by the angles $\alpha$ and $\beta$.

Previously, modeling of the SHG response was conducted only for heterostructures with a single ferroelectric phase [35,36,42,43]. In addition to the standard $a_1/a_2$ phase, our sample hosts a vortex phase as a second phase. We consider two models to describe our SHG polarimetry results: (1) a *one-phase model* that considers only the SHG response of the $a_1/a_2$ phase, and (2) a *two-phase model* that considers the independent and interfering SHG responses of the $a_1/a_2$ phase and the vortex phase. We compare the fits of these two models in Figs. 2 and 3 to answer: (a) If the one-phase model can already emulate the SHG response of the phase coexistence, and (b) if the two-phase model can appropriately describe the SHG polarimetry measurements.

In our models, we consider only the SHG response for the in-plane projection of the local polarization because of the normal-incidence geometry of our measurements. We further assume destructive interference of SHG responses of states with oppositely oriented polarization within either phase because of the phase difference of 180° [45]. Because of the large number of parameters the models were fitted to the SHG polarimetry results with a Monte Carlo-based approach. Specifically, we used a dual-annealing algorithm as implemented in SCIPY's optimization library [46]. This algorithm can find the global minimum of a function, and we make use of it by minimizing the residual sum of squares of the measured and the modeled intensity. We will now move on to derive explicit expressions for the ISHG intensity.

### 1. One-phase model

In the one-phase model of the SHG response of the $a_1/a_2$ phase, the SHG contributions for a local spontaneous polarization along [100] and [010] have equal spectral dependence of the $\hat{\chi}^{(2)}$ tensor components. We describe the fractions of the regions with local polarization pointing towards [100], [$\bar{1}$00], [010], and [0$\bar{1}$0] with parameters $A_1^+$, $A_1^-$, $A_2^+$, and $A_2^-$, respectively. We express the relative fractions of
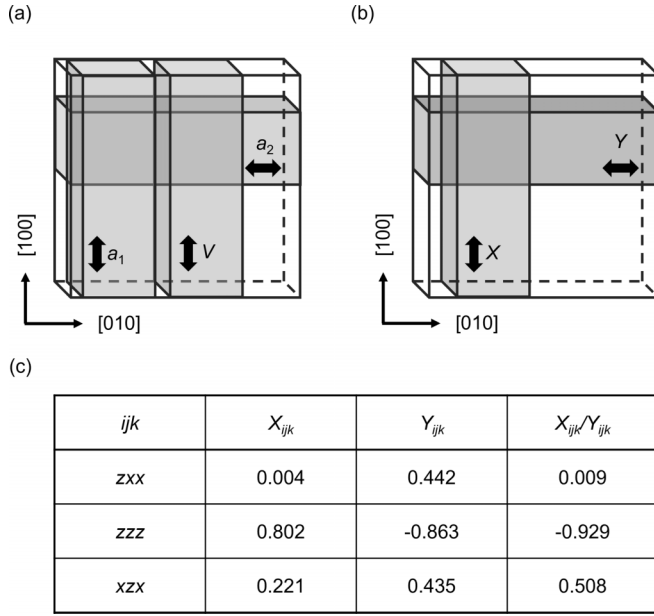
FIG. 3. (a) Schematic of the orientation of the net polarization for the $a_1$ domains, the $a_2$ domains, and the vortex phase ($V$). (b) Schematic relating the direction of the local spontaneous polarization to the parameters $X_{ijk}$ and $Y_{ijk}$ introduced to model the SHG response. The maximum SHG yield of the sample obtained upon variation of $\alpha$ and $\beta$ is set to a value of 1. (c) Values of $X_{ijk}$ and $Y_{ijk}$ parameters obtained from fitting of Eq. (9) as well as their ratio $X_{ijk}/Y_{ijk}$.

SHG signals originating from the $a_1$ and $a_2$ domains as $A_1$ and $A_2$, respectively, where $A_1 + A_2 = 1$. This leads to

$$A_1 = \frac{A_1^+ - A_1^-}{(A_1^+ - A_1^-) + (A_2^+ - A_2^-)}, \tag{2}$$

$$A_2 = \frac{A_2^+ - A_2^-}{(A_1^+ - A_1^-) + (A_2^+ - A_2^-)}. \tag{3}$$

The SHG intensity as a function of $\alpha$ and $\beta$ angles is then

$$\begin{aligned} I^{2\omega}(\alpha, \beta) = |A_1[&-(\chi_{zxx}\cos^2\alpha + \chi_{zzz}\sin^2\alpha)\sin\beta \\ &+ 2\chi_{xzx}\cos\alpha\sin\alpha\cos\beta] \\ + A_2[&-2\chi_{xzx}\cos\alpha\sin\alpha\sin\beta \\ &+ (\chi_{zxx}\sin^2\alpha + \chi_{zzz}\cos^2\alpha)\cos\beta]|^2. \end{aligned} \tag{4}$$

Fits of Eq. (4) to the data [gray lines in Figs. 2(b) and 2(c)] show that the one-phase model cannot satisfactorily describe the observed SHG polarimetry data of our PTO|STO superlattice even when considering a tensor $\hat{\chi}^{(2)}$ with real and imaginary components. This clearly confirms that our sample exhibits the suspected coexistence of (at least) two phases. We, thus, move onto the two-phase model to test whether it can appropriately model the SHG polarimetry measurements.

### 2. Two-phase model

We next consider the two-phase model in which the SHG contributions of the two phases have different spectral dependences, denoted with components $\chi_{ijk}$ for the $a_1/a_2$ phase and $\chi'_{ijk}$ for the vortex phase. For the $a_1/a_2$ phase, we again

describe the fractions of the regions with local polarization pointing towards [100], [$\bar{1}$00], [010], and [0$\bar{1}$0] with parameters $A_1^+, A_1^-, A_2^+$, and $A_2^-$, respectively. For the net polarization of the vortex phase, we describe the respective fractions of the regions with local polarization pointing towards [100] and [$\bar{1}$00] with parameters $V^+$ and $V^-$, respectively. We express the relative fractions of SHG signals originating from the $a_1$ domains as $A_1$, from the $a_2$ domains as $A_2$, and from the vortex phase as $V$, where $A_1 + A_2 + V = 1$. Specifically, we have

$$A_1 = \frac{A_1^+ - A_1^-}{(A_1^+ - A_1^-) + (A_2^+ - A_2^-) + (V^+ - V^-)}, \tag{5}$$

$$A_2 = \frac{A_2^+ - A_2^-}{(A_1^+ - A_1^-) + (A_2^+ - A_2^-) + (V^+ - V^-)}, \tag{6}$$

$$V = \frac{V^+ - V^-}{(A_1^+ - A_1^-) + (A_2^+ - A_2^-) + (V^+ - V^-)}. \tag{7}$$

This leads to a SHG intensity in our polarimetry measurements according to

$$\begin{aligned} I^{2\omega}(\alpha, \beta) = |A_1[&-(\chi_{zxx}\cos^2\alpha + \chi_{zzz}\sin^2\alpha)\sin\beta \\ &+ 2\chi_{xzx}\cos\alpha\sin\alpha\cos\beta] \\ + V[&-(\chi'_{zxx}\cos^2\alpha + \chi'_{zzz}\sin^2\alpha)\sin\beta \\ &+ 2\chi'_{xzx}\cos\alpha\sin\alpha\cos\beta] \\ + A_2[&-2\chi_{xzx}\cos\alpha\sin\alpha\sin\beta \\ &+ (\chi_{zxx}\sin^2\alpha + \chi_{zzz}\cos^2\alpha)\cos\beta]|^2. \end{aligned} \tag{8}$$

Because the SHG contributions of the $a_1$ domains and the net axial polarization of the vortex phase have an equivalent angular dependence on $\alpha$ and $\beta$ [Eq. (8)], we need to consider these SHG contributions with a single set of parameters. We, therefore, define the $X$ parameters as $X_{ijk} = A_1\chi_{ijk} + V\chi'_{ijk}$. Equivalently, for the $a_2$ domains, we define $Y$ parameters as $Y_{ijk} = A_2\chi_{ijk}$, see Figs. 3(a) and 3(b). The final expression for the SHG intensity in our polarimetry measurements [black lines in Figs. 2(b) and 2(c)] is then

$$\begin{aligned} I^{2\omega}(\alpha, \beta) = |&-(X_{zxx}\cos^2\alpha + X_{zzz}\sin^2\alpha)\sin\beta \\ &+ 2X_{xzx}\cos\alpha\sin\alpha\cos\beta \\ &- 2Y_{xzx}\cos\alpha\sin\alpha\sin\beta \\ &+ (Y_{zxx}\sin^2\alpha + Y_{zzz}\cos^2\alpha)\cos\beta)|^2. \end{aligned} \tag{9}$$

We see in Fig. 2 (black lines) that the two-phase model reproduces the results of our SHG polarimetry very well. The $X$ and $Y$ values used in the fitting are listed in Fig. 3(c). We next test the spectral dependence of the SHG responses of the $a_1/a_2$ phase and the vortex phase by scrutinizing the ratios of $X$ and $Y$ parameters: $X_{ijk}/Y_{ijk} = (A_1\chi_{ijk} + V\chi'_{ijk})/A_2\chi_{ijk}$. If the two phases were associated with the same SHG spectral dependence, the ratio would be equal for any set of $i, j, k$,

$$\frac{X_{ijk}}{Y_{ijk}} \equiv \frac{A_1 + V}{A_2}. \tag{10}$$

However, we observe drastic variations of $X_{ijk}/Y_{ijk}$ including a sign reversal in Fig. 3(c), showing that the SHG reponses of the $a_1/a_2$ phase and the vortex phase have different spectral
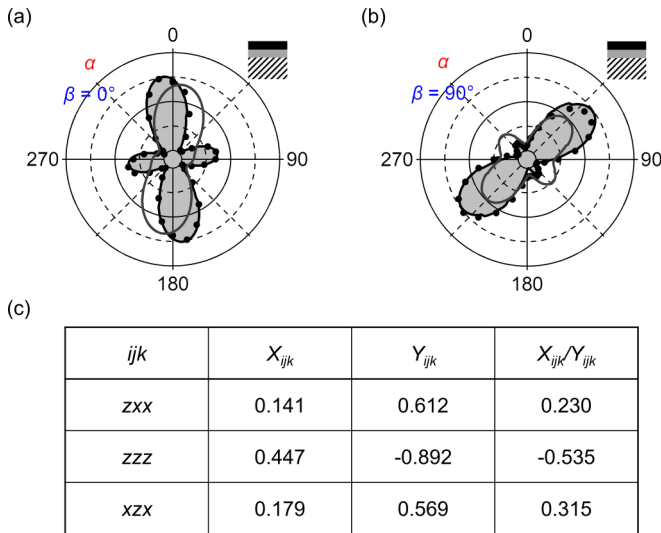
FIG. 4. (a) and (b) Polar plots of the SHG intensity (points) versus the incident-light polarization angle $\alpha$ for a single STO-capped PTO layer with (a) $\beta = 0°$ and (b) $\beta = 90°$. Gray lines are fits of the one-phase model based on Eq. (4), and black lines are fits of the two-phase model based on Eq. (9). A schematic of the heterostructure is given as inset on the top right. Gray denotes PTO, black denotes STO, and upward hatching denotes the SRO-buffered DSO substrate. The intensity scale is equal in (a) and (b). (c) Values of $X_{ijk}$ and $Y_{ijk}$ obtained from fitting Eq. (9) for the case of a single STO-capped PTO layer as well as their ratio $X_{ijk}/Y_{ijk}$.

| $ijk$ | $X_{ijk}$ | $Y_{ijk}$ | $X_{ijk}/Y_{ijk}$ |
|---|---|---|---|
| $zxx$ | 0.141 | 0.612 | 0.230 |
| $zzz$ | 0.447 | -0.892 | -0.535 |
| $xzx$ | 0.179 | 0.569 | 0.315 |

dependences. This points to the very different microscopy of the electronic transitions and interactions establishing the two phases.

## C. Observation of interlayer coupling in PTO|STO heterostructures

The PTO|STO superlattice architecture is commonly selected to increase the ferroelectric volume so that the signals probing the ferroelectric state become measurable, whereas assuming that the characteristic features of a single STO-capped PTO layer remain preserved. Using the extreme sensitivity of the SHG polarimetry, we will now verify to what extent the phase coexistence of the $a_1/a_2$ phase and the vortex phase in a single STO-capped PTO layer is, in fact, equivalent to that in the superlattice with multiple PTO|STO repetitions. The results of SHG polarimetry on a the single STO-capped PTO layer are shown in Figs. 4(a) and 4(b), and they are qualitatively similar to the results of the SHG polarimetry of the superlattice in Fig. 2. By modeling the SHG polarimetry for the STO-capped PTO layer following the procedure described for Fig. 3, we again find that only the two-phase model appropriately describes the measured SHG data, see Fig. 4. This confirms the presence of the vortex phase in coexistence with the $a_1/a_2$ phase even in a single STO-capped PTO layer, in agreement with the Ref. [9]. Although it seems that as anticipated, the supperlattice behaves as "many STO-capped PTO layers," there is one interesting detail where this scaling effect does not hold.

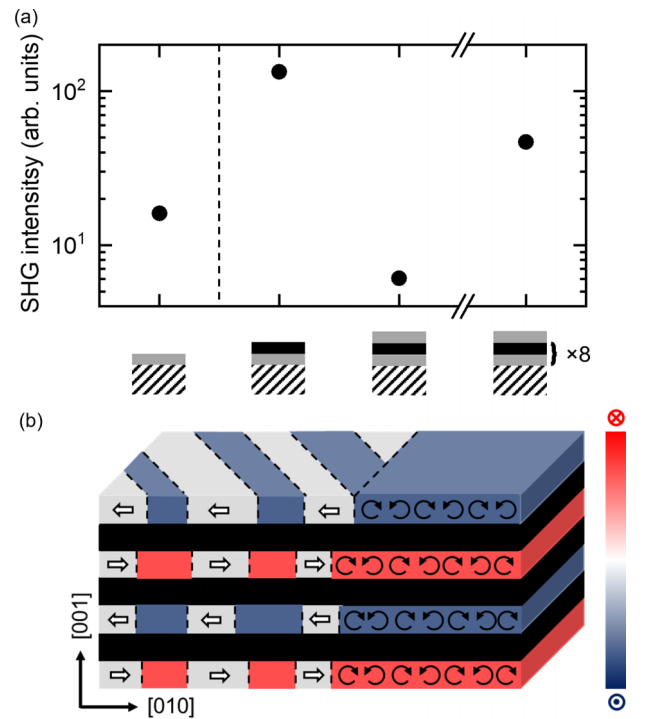Surprisingly, despite identical laser-excitation parameters, the SHG yield of a $(PTO|STO)_8|PTO$ superlattice is lower



FIG. 5. (a) SHG intensity integrated over $\alpha$ for SHG polarimetry at $\beta = 0°$ as in Figs. 2(b) and 4(a) for an uncapped PTO reference layer, a STO-capped PTO layer (PTO|STO heterostructure with an odd number of PTO layers), a PTO|STO|PTO multilayer (PTO|STO heterostructure with an even number of PTO layers), and a $(PTO|STO)_8|PTO$ superlattice (PTO|STO heterostructure with an odd number of PTO layers), see the schematics. Gray denotes PTO, black denotes STO, and upward hatching denotes the SRO-buffered DSO substrate. The downward-hatched area corresponds to the background SHG intensity measured from the DSO substrate. To ensure quantitative comparability of the SHG yield of different samples, the SHG signal is normalized to a reference SHG signal gained from a SHG-active reference quartz crystal in each case. (b) Conceptual sketch of locally reversed polarization in neighboring PTO layers. Gray, blue, and red denote PTO, and black denotes STO. Straight arrows represent the $a_1/a_2$ phase, and the curved arrows represent the vortex phase.

than that of a single STO-capped PTO layer even though the amount of ferroelectric material in the superlattice exceeds that of the STO-capped PTO layer by a factor of 9, see Fig. 5. Such a dependence is in striking contradiction to the understanding that a superlattice architecture would increase the measured signals proportionally to the increase in the volume of ferroelectric material. For an explanation of this discrepancy, we recall that the SHG emission is sensitive to the sign of polarization. Specifically, PTO layers with opposite polarization directions will emit SHG light waves with a $180°$-phase difference that would cancel out in superposition. The two times smaller SHG yield of the superlattice compared to the SHG yield of the STO-capped PTO layer points exactly to such a cancellation between SHG waves originating in different PTO layers of the superlattice [45]. In order to verify this assumption, we compare the SHG yield of PTO|STO heterostructures with a different number of periods. Specifically, we integrate the signal of the SHG polarimetry data for

$\beta = 0°$ for an uncapped PTO layer, a single STO-capped PTO layer, a PTO|STO|PTO multilayer, and a (PTO|STO)$_8$|PTO superlattice, see Fig. 5(a).

The SHG yield of an uncapped PTO layer as our system of reference is low because the polarization is predominantly oriented out of plane [47,48] and is, thus, not captured in our in-plane-polarization-sensitive measurement configuration [41]. For the single STO-capped PTO layer, in-plane-polarized domains and vortices form in the PTO layer which results in a ten times higher SHG yield than in the case of an uncapped PTO layer. Surprisingly, when another PTO layer is added on top, the SHG yield in the resulting PTO|STO|PTO multilayer decreases by a factor of 20, yet maintains a similar polarimetric dependence as the single STO-capped PTO layer in the Supplemental Material [22]. We verified this behavior in more than ten samples of STO-capped PTO layers and PTO|STO|PTO multilayers. Such low SHG yield of the PTO|STO|PTO multilayer could point to destructive interference of SHG waves originating from neighboring PTO layers. This implies an antiparallel arrangement of in-plane polarization components of the $a_1/a_2$ phase and the vortex phase in consecutive layers. Most likely, electrostatic and elastic interactions in the form of a dipolar coupling and electrostriction, respectively, on the local scale induce a spatial correlation of in-plane-polarized domains with oppositely oriented polarizations in the direction normal to the heterostructure plane [13,49,50] as sketched in Fig. 5(b). By reinvoking that the SHG yield of a superlattice is comparable to the SHG yield of a single STO-capped PTO layer, we conclude that an alternating high and low SHG yield with the number of PTO layers is universal rather than restricted to a certain number of PTO layers. Specifically, in the case of in-plane polarized heterostructures (at least one capped PTO layer), the SHG yield is more than ten times larger from samples with an odd number of PTO layers than from samples with an even number of PTO layers. Our noninvasive approach, thus, unambiguously identifies not only the phase coexistence in each layer, but also an additional spatial correlation between in-plane polarized domains with oppositely oriented polarizations across the layers.

## IV. CONCLUSION

To summarize, using a noninvasive optical approach, we identified a phase coexistence of the polar $a_1/a_2$ phase and the polar vortex phase in PTO|STO heterostructures. SHG polarimetry evidences the presence of such as phase coexistence even in a single STO-capped PTO layer. Furthermore, by measuring the SHG yield of a series of PTO|STO heterostructures in dependence of the number of PTO and STO layers, we find an interlayer coupling effect between neighboring PTO layers that leads to a spatial correlation of in-plane polarized domains with oppositely oriented polarizations in successive layers. Specifically, this arrangement of polarization in neighboring PTO layers of PTO|STO heterostructures results in a SHG yield which is is an order of magnitude larger for an odd number of PTO layers than for an even number of PTO layers. We expect that our noninvasive optical approach could be used as a convenient tool in identifying complex phases in oxide-electronic materials and permit operando monitoring of the evolution of complex ordered phases under electric fields, an important prerequisite for promoting these systems towards device functionality [17–21].

All authors discussed the results. N.S., M.T., and M.F. wrote the paper. N.S. performed the thin-film growth, PFM, XRD, and SHG measurements. N.S. and A.B. developed the models for fitting the SHG measurements and A.B. performed the Monte Carlo simulations. M.C. and M.D.R. carried out the STEM investigation. N.S. and M.T. designed the experiment. M.T. supervised the work jointly with M.F.

[1] Y. L. Tang, Y. L. Zhu, X. L. Ma, A. Y. Borisevich, A. N. Morozovska, E. A. Eliseev, W. Y. Wang, Y. J. Wang, Y. B. Xu, Z. D. Zhang, and S. J. Pennycook, Observation of a periodic array of flux-closure quadrants in strained ferroelectric PbTiO$_3$ films, Science **348**, 547 (2015).

[2] S. Li, Y. L. Zhu, Y. J. Wang, Y. L. Tang, Y. Liu, S. R. Zhang, J. Y. Ma, and X. L. Ma, Periodic arrays of flux-closure domains in ferroelectric thin films with oxide electrodes, Appl. Phys. Lett. **111**, 52901 (2017).

[3] A. K. Yadav, C. T. Nelson, S. L. Hsu, Z. Hong, J. D. Clarkson, C. M. Schlepüetz, A. R. Damodaran, P. Shafer, E. Arenholz, L. R. Dedon, D. Chen, A. Vishwanath, A. M. Minor, L. Q. Chen, J. F. Scott, L. W. Martin, and R. Ramesh, Observation of polar vortices in oxide superlattices, Nature (London) **530**, 198 (2016).

[4] Z. Hong, A. R. Damodaran, F. Xue, S.-L. Hsu, J. Britson, A. K. Yadav, C. T. Nelson, J.-J. Wang, J. F. Scott, L. W. Martin, R. Ramesh, and L.-Q. Chen, Stability of polar vortex lattice in ferroelectric superlattices, Nano Lett. **17**, 2246 (2017).

[5] A. R. Damodaran, J. D. Clarkson, Z. Hong, H. Liu, A. K. Yadav, C. T. Nelson, S.-L. Hsu, M. R. McCarter, K.-D. Park, V. Kravtsov, A. Farhan, Y. Dong, Z. Cai, H. Zhou, P. Aguado-Puente, P. Garcia-Fernandez, J. Iñiguez, J. Junquera, A. Scholl, M. B. Raschke *et al.*, Phase coexistence and electric-field control of toroidal order in oxide superlattices, Nature Mater. **16**, 1003 (2017).

[6] S. Das, Y. L. Tang, Z. Hong, M. A. P. Gonçalves, M. R. McCarter, C. Klewe, K. X. Nguyen, F. Gómez-Ortiz, P. Shafer, E. Arenholz, V. A. Stoica, S.-L. Hsu, B. Wang, C. Ophus,

J. F. Liu, C. T. Nelson, S. Saremi, B. Prasad, A. B. Mei, D. G. Schlom *et al.*, Observation of room-temperature polar skyrmions, Nature (London) **568**, 368 (2019).

[7] V. A. Stoica, N. Laanait, C. Dai, Z. Hong, Y. Yuan, Z. Zhang, S. Lei, M. R. McCarter, A. Yadav, A. R. Damodaran, S. Das, G. A. Stone, J. Karapetrova, D. A. Walko, X. Zhang, L. W. Martin, R. Ramesh, L.-Q. Chen, H. Wen, V. Gopalan *et al.*, Optical creation of a supercrystal with three-dimensional nanoscale periodicity, Nature Mater. **18**, 377 (2019).

[8] Y. Sun, A. Y. Abid, C. Tan, C. Ren, M. Li, N. Li, P. Chen, Y. Li, J. Zhang, X. Zhong, J. Wang, M. Liao, K. Liu, X. Bai, Y. Zhou, D. Yu, and P. Gao, Subunit cell–level measurement of polarization in an individual polar vortex, Sci. Adv. **5**, eaav4355 (2019).

[9] S.-L. Hsu, M. R. McCarter, C. Dai, Z. Hong, L.-Q. Chen, C. T. Nelson, L. W. Martin, and R. Ramesh, Emergence of the vortex state in confined ferroelectric heterostructures, Adv. Mater. **31**, 1901014 (2019).

[10] Y. J. Wang, Y. P. Feng, Y. L. Zhu, Y. L. Tang, L. X. Yang, M. J. Zou, W. R. Geng, M. J. Han, X. W. Guo, B. Wu, and X. L. Ma, Polar meron lattice in strained oxide ferroelectrics, Nature Mater. **19**, 881 (2020).

[11] S. Das, Z. Hong, M. McCarter, P. Shafer, Y.-T. Shao, D. A. Muller, L. W. Martin, and R. Ramesh, A new era in ferroelectrics, APL Mater. **8**, 120902 (2020).

[12] S. Chen, S. Yuan, Z. Hou, Y. Tang, J. Zhang, T. Wang, K. Li, W. Zhao, X. Liu, L. Chen, L. W. Martin, and Z. Chen, Recent progress on topological structures in ferroic thin films and heterostructures, Adv. Mater. **33**, 2000857 (2020).

[13] Y. Liu, Y.-J. Wang, Y.-L. Zhu, C.-H. Lei, Y.-L. Tang, S. Li, S.-R. Zhang, J. Li, and X.-L. Ma, Large scale two-dimensional flux-closure domain arrays in oxide multilayers and their controlled growth, Nano Lett. **17**, 7258 (2017).

[14] N. Strkalj, E. Gradauskaite, J. Nordlander, and M. Trassin, Design and manipulation of ferroic domains in complex oxide heterostructures, Materials **12**, 3108 (2019).

[15] Y. L. Tang, Y. L. Zhu, and X. L. Ma, Topological polar structures in ferroelectric oxide films, J. Appl. Phys. **129**, 200904 (2021).

[16] N. Strkalj, M. Bernet, M. F. Sarott, J. Schaab, T. Weber, M. Fiebig, and M. Trassin, Stabilization and manipulation of in-plane polarization in a ferroelectric|dielectric superlattice, J. Appl. Phys. **129**, 174104 (2021).

[17] S. Salahuddin and S. Datta, Use of negative capacitance to provide voltage amplification for low power nanoscale devices, Nano Lett. **8**, 405 (2008).

[18] A. I. Khan, K. Chatterjee, B. Wang, S. Drapcho, L. You, C. Serrao, S. R. Bakaul, R. Ramesh, and S. Salahuddin, Negative capacitance in a ferroelectric capacitor, Nature Mater. **14**, 182 (2015).

[19] P. Zubko, J. C. Wojdeł, M. Hadjimichael, S. Fernandez-Peña, A. Sené, I. Luk'yanchuk, J.-M. Triscone, and J. Íñiguez, Negative capacitance in multidomain ferroelectric superlattices, Nature (London) **534**, 524 (2016).

[20] A. K. Yadav, K. X. Nguyen, Z. Hong, P. García-Fernández, P. Aguado-Puente, C. T. Nelson, S. Das, B. Prasad, D. Kwon, S. Cheema, A. I. Khan, C. Hu, J. Íñiguez, J. Junquera, L.-Q. Chen, D. A. Muller, R. Ramesh, and S. Salahuddin, Spatially resolved steady-state negative capacitance, Nature (London) **565**, 468 (2019).

[21] J. Iñiguez, P. Zubko, I. Luk'yanchuk, and A. Cano, Ferroelectric negative capacitance, Nat. Rev. Mater. **4**, 243 (2019).

[22] See Supplemental Material at http://link.aps.org/supplemental/10.1103/PhysRevB.105.174101 for time-dependent RHEED intensity during pulsed laser deposition, topography, lateral PFM response of the as-grown state, and XRD characterization of the phase coexistence in the PTO|STO superlattice on SRO-buffered DSO. It further includes SHG polarimetry of the uncapped PTO layer and the PTO|STO|PTO multilayer.

[23] L. Jones, H. Yang, T. J. Pennycook, M. S. J. J. Marshall, S. Van Aert, N. D. Browning, M. R. Castell, and P. D. Nellist, Smart Align-A new tool for robust non-rigid registration of scanning microscopy data, Adv. Struct. Chem. Imaging **1**, 8 (2015).

[24] H. Du, A nonlinear filtering algorithm for denoising HR(S)TEM micrographs., Ultramicroscopy **151**, 62 (2015).

[25] A. B. Yankovich, B. Berkels, W. Dahmen, P. Binev, S. I. Sanchez, S. A. Bradley, A. Li, I. Szlufarska, and P. M. Voyles, Picometre-precision analysis of scanning transmission electron microscopy images of platinum nanocatalysts, Nat. Commun. **5**, 4155 (2014).

[26] S. Prosandeev, I. I. Naumov, H. Fu, L. Bellaiche, M. P. D. Campbell, R. G. P. McQuaid, L.-W. Chang, A. Schilling, L. J. McGilly, A. Kumar, and J. Marty Gregg, *Nanoscale Ferroelectrics and Multiferroics* (Wiley, Hoboken, NJ, 2016), pp. 700–728.

[27] P. Shafer, P. García-Fernández, P. Aguado-Puente, A. R. Damodaran, A. K. Yadav, C. T. Nelson, S.-L. Hsu, J. C. Wojdeł, J. Íñiguez, L. W. Martin, E. Arenholz, J. Junquera, and R. Ramesh, Emergent chirality in the electric polarization texture of titanate superlattices, Proc. Natl. Acad. Sci. USA **115**, 915 (2018).

[28] S. A. Denev, T. T. A. Lummen, E. Barnes, A. Kumar, and V. Gopalan, Probing ferroelectrics using optical second harmonic generation, J. Am. Ceram. Soc. **94**, 2699 (2011).

[29] J. Nordlander, G. De Luca, N. Strkalj, M. Fiebig, and M. Trassin, Probing ferroic states in oxide thin films using optical second harmonic generation, Appl. Sci. **8**, 570 (2018).

[30] A. Prylepa, C. Reitböck, M. Cobet, A. Jesacher, X. Jin, R. Adelung, M. Schatzl-Linder, G. Luckeneder, K.-H. Stellnberger, T. Steck, J. Faderl, T. Stehrer, and D. Stifter, Material characterisation with methods of nonlinear optics, J. Phys. D: Appl. Phys. **51**, 043001 (2018).

[31] V. Gopalan and R. Raj, Domain structure-second harmonic generation correlation in potassium niobate thin films deposited on a strontium titanate substrate, J. Am. Ceram. Soc. **79**, 3289 (1996).

[32] C. J. Roh, S. Y. Hamh, C.-S. Woo, K.-E. Kim, C.-H. Yang, and J. S. Lee, Ferroelectric domain states of a tetragonal $BiFeO_3$ thin film investigated by second harmonic generation microscopy, Nanoscale Res. Lett. **12**, 353 (2017).

[33] M. Trassin, G. D. Luca, S. Manz, and M. Fiebig, Probing ferroelectric domain engineering in $BiFeO_3$ thin films by second harmonic generation, Adv. Mater. **27**, 4871 (2015).

[34] Y. Zhang, Y. Zhang, Q. Guo, X. Zhong, Y. Chu, H. Lu, G. Zhong, J. Jiang, C. Tan, M. Liao, Z. Lu, D. Zhang, J. Wang, J. Yuan, and Y. Zhou, Characterization of domain distributions by second harmonic generation in ferroelectrics, npj Comput. Mater. **4**, 39 (2018).

[35] J.-S. Wang, K.-J. Jin, H.-Z. Guo, J.-X. Gu, Q. Wan, X. He, X.-L. Li, X.-L. Xu, and G.-Z. Yang, Evolution of structural distortion

in $BiFeO_3$ thin films probed by second-harmonic generation, Sci. Rep. **6**, 38268 (2016).

[36] A. Kumar, S. Denev, R. J. Zeches, E. Vlahos, N. J. Podraza, A. Melville, D. G. Schlom, R. Ramesh, and V. Gopalan, Probing mixed tetragonal/rhombohedral-like monoclinic phases in strained bismuth ferrite films by optical second harmonic generation, Appl. Phys. Lett. **97**, 112903 (2010).

[37] N. Strkalj, G. De Luca, M. Campanini, S. Pal, J. Schaab, C. Gattinoni, N. A. Spaldin, M. D. Rossell, M. Fiebig, and M. Trassin, Depolarizing Field Effects in Epitaxial Capacitor Heterostructures, Phys. Rev. Lett. **123**, 147601 (2019).

[38] N. Strkalj, C. Gattinoni, A. Vogel, M. Campanini, R. Haerdi, A. Rossi, M. D. Rossell, N. A. Spaldin, M. Fiebig, and M. Trassin, *In-situ* monitoring of interface proximity effects on polarization in ultrathin ferroelectrics, Nat. Commun. **11**, 5815 (2020).

[39] M. F. Sarott, M. Fiebig, and M. Trassin, Tracking ferroelectric domain formation during epitaxial growth of $PbTiO_3$ films, Appl. Phys. Lett. **117**, 132901 (2020).

[40] S. Cherifi-Hertel, H. Bulou, R. Hertel, G. Taupier, K. D. H. Dorkenoo, C. Andreas, J. Guyonnet, I. Gaponenko, K. Gallo, and P. Paruch, Non-Ising and chiral ferroelectric domain walls revealed by nonlinear optical microscopy, Nat. Commun. **8**, 15768 (2017).

[41] G. De Luca, M. D. Rossell, J. Schaab, N. Viart, M. Fiebig, and M. Trassin, Domain wall architecture in tetragonal ferroelectric thin films, Adv. Mater. **29**, 1605145 (2017).

[42] V. Gopalan and R. Raj, Domain structure and phase transitions in epitaxial $KNbO_3$ thin films studied by in situ second harmonic generation measurements, Appl. Phys. Lett. **68**, 1323 (1996).

[43] J. Nordlander, F. Eltes, M. Reynaud, J. Nürnberg, G. De Luca, D. Caimi, A. A. Demkov, S. Abel, M. Fiebig, J. Fompeyrine, and M. Trassin, Ferroelectric domain architecture and poling of $batio_3$ on si, Phys. Rev. Material **4**, 034406 (2020).

[44] R. R. Birss, *Symmetry and Magnetism* (North-Holland, Amsterdam, 1964).

[45] G. De Luca, N. Strkalj, S. Manz, C. Bouillet, M. Fiebig, and M. Trassin, Nanoscale design of polarization in ultrathin ferroelectric heterostructures, Nat. Commun. **8**, 1419 (2017).

[46] P. Virtanen, R. Gommers, T. E. Oliphant, M. Haberland, T. Reddy, D. Cournapeau, E. Burovski, P. Peterson, W. Weckesser, J. Bright, S. J. van der Walt, M. Brett, J. Wilson, K. J. Millman, N. Mayorov, A. R. J. Nelson, E. Jones, R. Kern, E. Larson, C. J. Carey *et al.*, SciPy 1.0: Fundamental algorithms for scientific computing in python, Nat. Methods **17**, 261 (2020).

[47] N. A. Pertsev and V. G. Koukhar, Polarization Instability in Polydomain Ferroelectric Epitaxial Thin Films and the Formation of Heterophase Structures, Phys. Rev. Lett. **84**, 3722 (2000).

[48] N. A. Pertsev, A. G. Zembilgotov, and A. K. Tagantsev, Effect of Mechanical Boundary Conditions on Phase Diagrams of Epitaxial Ferroelectric Thin Films, Phys. Rev. Lett. **80**, 1988 (1998).

[49] P. Zubko, N. Jecklin, A. Torres-Pardo, P. Aguado-Puente, A. Gloter, C. Lichtensteiger, J. Junquera, O. Stéphan, and J.-M. Triscone, Electrostatic coupling and local structural distortions at interfaces in ferroelectric|paraelectric superlattices, Nano Lett. **12**, 2846 (2012).

[50] V. A. Stephanovich, I. A. Luk'yanchuk, and M. G. Karkut, Domain-Enhanced Interlayer Coupling in Ferroelectric— Paraelectric Superlattices, Phys. Rev. Lett. **94**, 047601 (2005).